Inducing conductivity in polycrystalline ZnO 1- x thin films through space charge doping

Andrea Paradisi, Johan Biscaras, Abhay Shukla

Inducing conductivity in polycrystalline ZnO_{1-x} thin films through space charge doping

Andrea Paradisi, Johan Biscaras, and Abhay Shukla

Citation: Journal of Applied Physics **122**, 095301 (2017); doi: 10.1063/1.5001127
View online: http://dx.doi.org/10.1063/1.5001127
View Table of Contents: http://aip.scitation.org/toc/jap/122/9
Published by the American Institute of Physics

Inducing conductivity in polycrystalline ZnO_{1-x} thin films through space charge doping

Andrea Paradisi, Johan Biscaras, and Abhay Shukla[a)]
Institut de Minéralogie, de Physique des Matériaux et de Cosmochimie, Sorbonne Université Paris 06, UMR CNRS 7590, MNHN, IRD UMR 206, 4 Place Jussieu, F-75005 Paris, France

(Received 17 January 2017; accepted 19 August 2017; published online 5 September 2017)

We induce ultra-high carrier charge density in polycrystalline zinc oxide thin films on glass with a thickness of few tens of nm, achieving carrier concentrations as high as 2.2×10^{14} cm^{-2}, well beyond the Ioffe-Regel limit for an insulator-metal transition in two dimensions. The sheet resistance is consequently lowered by up to 5 orders of magnitude to about 2 k $\Omega/\square$ without alteration of transparency thanks to our *space charge doping* technique. Electrostatic doping of such a large band-gap semiconductor is quite challenging, and a high surface potential is required in order to induce conductivity at the interface. Through magneto-transport measurements performed at low temperature on the doped films, we show that both weak localization and weak anti-localization of charge carriers can be observed and that these quantum interference phenomena can be modulated by the carrier concentration and temperature. *Published by AIP Publishing.*
[http://dx.doi.org/10.1063/1.5001127]

I. INTRODUCTION

Zinc oxide (ZnO) is a wide band-gap semiconductor ($E_g \sim 3.3$ eV at 300 K)[1,2] transparent in the visible wavelength range. It has been widely studied in the past with the aim of fabricating transparent field-effect transistors[3,4] and optoelectronic devices[5,6] and creating surface quantum wells[7] or transparent conducting electrodes[8–10] with chemical doping. Magneto-transport and the study of phase breaking mechanisms such as spin relaxation in systems such as ZnO are motivated by potential applications for this material in spintronics.[11,12] Exposure of single crystal ZnO to atomic hydrogen,[13] low-energy hydrogen ion implantation,[14] and thermalized He^+ ions[15] can lead to extremely high electron concentrations at the sample surface[16] (up to 5×10^{14} cm^{-2}). Electrostatic methods involving a liquid dielectric and a double layer transistor have also been used to induce high carrier density on the surface of a ZnO sample.[17,18] The most widespread technique for doping ZnO is chemical doping with Al atoms. The resistivity can be lowered considerably, from 10^5 Ω·cm for the undoped crystal down to 10^{-4} Ω·cm in the doped case.[10,19] Chemical doping however introduces defects and alters the transparency of the sample, besides being irreversible.

We have introduced a technique called *Space Charge Doping* (SCD) and demonstrated that it is an extremely efficient tool for doping 2D materials deposited on a glass substrate[20,21] without compromising sample quality and ensuring reversibility and uniformity of doping. The technique exploits an intrinsic property of all commercial glasses: the presence of Na^+ ions in the amorphous SiO_2 network. Na^+ ions are located close to the non-bridging O^{2-} ions in the SiO_2 network, and their mobility, which is negligible at room temperature, increases exponentially by heating the glass.[22] If an electric field is applied perpendicular to the surface of a glass substrate, Na^+ ions will drift towards the cathode and accumulate beneath the surface, creating a positive space charge. At the anode, a Na^+ depleted region is formed, leaving the non-bridging oxygen ions of the SiO_2 network uncompensated and creating a negative space charge. Cooling the glass to room temperature lowers the Na^+ ion mobility to negligible values, thus freezing and preserving the space charge even in the absence of V_G. A material deposited on the glass surface will thus experience a strong electric field created by this space charge, and the consequent band bending at the interface will result in *n*-doping for Na^+ accumulation or *p*-doping for Na^+ depletion as in the channel of a field effect transistor (FET). However, SCD can induce carrier concentrations beyond 10^{14} cm^{-2}, an order of magnitude higher than in the FETs, as we shall see below.

In this work, we apply SCD on polycrystalline ZnO_{1-x} thin films. The fabrication technique and eventual post-annealing result in a change in stoichiometry due to oxygen vacancies.[10,23,24] We show that our SCD technique is able to remarkably enhance the carrier concentration and thus lower the sheet resistance of samples by several order of magnitudes (up to 5 in some cases) in a reversible way and without damaging the samples. Through low-temperature magneto-transport measurements, we determine the dominant scattering mechanisms in the thin films and deduce that the electrostatically induced charge carriers are confined in two dimensions at the glass/ZnO interface. Moreover, we show that the properties of the doped samples are independent of the initial stoichiometry and thickness and that the spin relaxation time can be modulated by the doping induced by the space charge.

II. METHODS

ZnO thin films were deposited on soda-lime glass substrates with room temperature RF magnetron sputtering of a Zn target in the presence of Ar and O. The total pressure in

a)Electronic mail: abhay.shukla@upmc.fr

the chamber during the deposition was kept at 10^{-2} mbar, while the partial pressure of Ar and O was varied ($P_{Ar} = 80\%$ and $P_O = 20\%$ or $P_{Ar} = 76\%$ and $P_O = 24\%$) to modulate the oxygen content and the n doping in ZnO. By varying the deposition time, films with a thickness between 7.5 and 40 nm were grown as determined by Atomic Force Microscopy (AFM). Structural analysis was done with AFM and grazing incidence X-ray diffraction (XRD) with an incidence angle of 4° using a Cu source (the wavelength of the X-ray is $\lambda = 0.15405980$ nm). An eventual high temperature vacuum annealing (623 K) was used to decrease the initial sample resistance probably through oxygen vacancies.

Electronic transport measurements as a function of space charge doping were made in a custom-made cryostat capable of reaching temperatures in the range of 3–420 K with the possibility of applying an external magnetic field of ±2 T. Samples were shaped into circles of ∼2 mm diameter by covering the center with a drop of poly(methyl methacrylate) (PMMA) and immersing it in an aqueous solution of HCl (15%) for ∼7 s in order to etch the uncovered zinc oxide. The contact deposition was done by thermal evaporation of gold through a steel stencil mask previously aligned to the sample, thus avoiding a lithography step and related surface contamination with polymers. Gold contacts (100 nm thick) were placed at the edge of the sample in a square van der Pauw geometry.

III. RESULTS AND DISCUSSION

A. Space charge doping of the samples

We focus on four samples labelled A, B, C, and D whose deposition parameters and thickness are listed in Table I. The X-ray diffraction spectra of the samples as deposited are shown in Fig. 1(a). The spectra are normalized with respect to the principal (002) reflection peak at 34.2° $< 2\theta <$ 34.6°, indicating texture with a preferential (00l) orientation,[25,26] and also show a much smaller feature at $2\theta \approx 63°$ corresponding to the (103) reflection. Samples B, C, and D were vacuum annealed ($p \leq 10^{-6}$ mbar) at a temperature of 623 K for 15 h. This decreased the sheet resistance through O desorption and also improved the crystalline quality with a small increase in grain size (decrease in the peak width) and release of strain (peak shift) as seen in Fig. 1(b) for samples B and C. The average grain size perpendicular to the substrate plane as estimated from the Scherrer formula[27] varies from 12.9 nm (sample A) to 10.3 nm (sample D), respectively. Figure 2 shows a typical AFM scan (here from sample A) of surface topography. The average in-plane grain size is estimated to be ∼28 nm, and combining this with the

TABLE I. The deposition parameters of different samples studied.

Sample	Ar/O	Deposition time (s)	Thickness (nm)
A	76/24	120	40
B	76/24	66	23
C	80/20	66	24
D	80/20	25	7.5

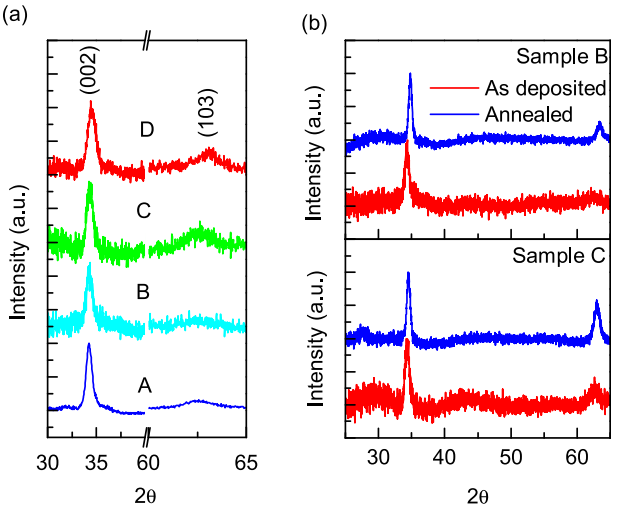

FIG. 1. (a) XRD spectra of the 4 analyzed samples measured as deposited and normalized with respect to the peak at 34°. (b) XRD spectra of Samples B and C before and after the vacuum annealing carried out at 623 K for 15 h.

XRD estimation, we conclude that grains have a disk-like shape oriented with (00l) planes parallel to the substrate.

We now describe the results of the electrostatic doping of ZnO thin films with the SCD technique, details of which can be found in our previous publications.[20,21] Our ZnO thin film samples show an initial sheet resistance, which depends on the oxygen content. Sample A has an initial sheet resistance (R_S) as high as 10^8 Ω/□, while the other vacuum annealed samples show an initial R_S of several tens of k Ω/□ before space charge doping. Figure 3 shows an example of the application of SCD on Sample A. It is first heated to the doping temperature of ∼370 K. A gate voltage of $V_G = +285$ V is then applied between the sample and the opposite face of the glass substrate. An abrupt drop in the resistance is observed as the space charge builds up with a fall of 4 orders of magnitude to $R_S \sim 14$ k Ω/□ in this particular case. When the desired value of R_S is reached, quenching the sample to room temperature freezes the space charge and fixes the carrier density, as shown in Fig. 4, where R_S vs T characteristics of samples A, B, C, and D are obtained at different carrier concentrations.

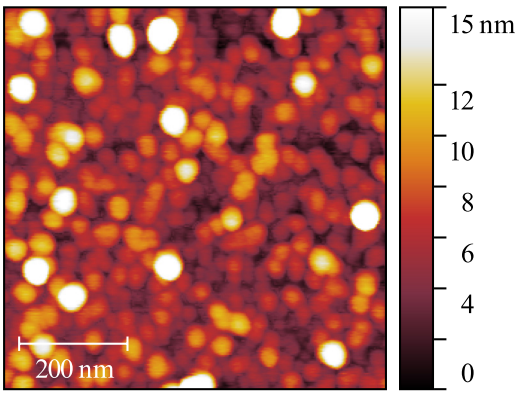

FIG. 2. AFM surface scan of a 40 nm thick ZnO film. The average grain size obtained from the measurement can be compared with the grain size obtained from the XRD analysis.

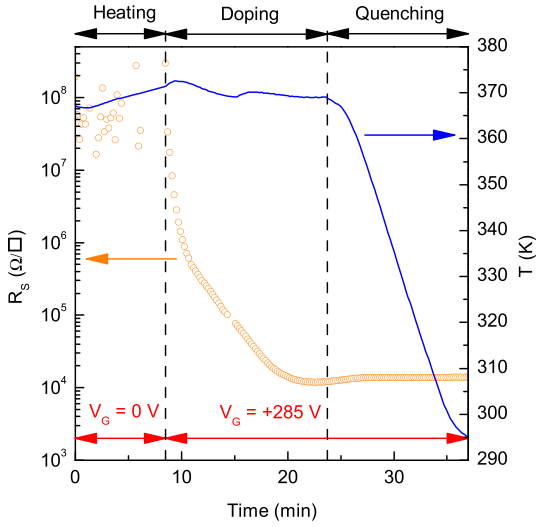

FIG. 3. Space charge doping of sample A. The initial sheet resistance of the sample was $R_S \approx 10^8\ \Omega/\square$. The sample is first heated at ∼370 K, and then, a gate voltage $V_G = +285$ V is applied. As observed, the space charge of Na^+ ions at the interface between the glass and the ZnO thin film causes a massive drop in R_S of ∼4 orders of magnitude.

We observe that the samples can be doped reversibly and that despite the different initial stoichiometry and thickness, the variation of the sheet resistance with doping and the maximum carrier concentration achieved, between 1.51 and $2.19 \times 10^{14}\,cm^{-2}$, are similar in all samples. Since the sample thickness varies from 7 to 40 nm, the doped layer is confined to a few nm and the intrinsic chemical doping does not influence electrostatic doping. The minimum value of R_S attained is also similar for all the samples, being of the order of 2 k Ω/□. This opens the possibility of use of this technique in applications such as transparent conductors by addressing practical questions such as stability and contact resistance. According to the Ioffe-Regel criterion,[28,29] the insulator to metal transition is marked by a critical carrier density n_c for which the product $k_F l_{tr} \geq 1$, with k_F being the Fermi wavevector and l_{tr} the mean free path. In our samples, for high doping, *i.e.*, $n_S > 10^{14}$ cm^{-2}, we obtain $k_F l_{tr} \gg 1$, with values varying between 21 and 42. At lower doping ($2.4–6.3 \times 10^{13}\,cm^{-2}$), $k_F l_{tr}$ is of the order of unity, ranging between 0.5 and 5.4. These values indicate that quantum interference may be important in our samples. In the high carrier density regime, where $k_F l_{tr} \gg 1$, $\partial R_S/\partial T$, however, remains negative (Fig. 4). We now identify the dominant scattering mechanism through the temperature dependence of the Hall mobility, assuming that in a polycrystalline thin film, the total mobility μ of the charge carriers is limited by scattering from grain boundaries (μ_{gb}), lattice phonons (μ_{ph}), and ionized impurities (μ_i), each of which has a characteristic temperature dependence,[30]

$$\frac{1}{\mu} = \frac{1}{\mu_{gb}} + \frac{1}{\mu_{ph}} + \frac{1}{\mu_i}. \tag{1}$$

The phonon contribution is negligible in our case as T ≤ 50 K. The grain boundary contribution to the mobility is given by[31]

$$\mu_{gb} = \mu_0 T^{-1/2} e^{-\phi_b/k_B T}, \tag{2}$$

where ϕ_b is the potential barrier height at the grain boundary and μ_0 is the mobility inside the grain. This implies a linear dependence of $\ln(\mu T^{1/2})$ on $1/T$, not observed in Fig. 5(a). The remaining scattering contribution, due to ionized impurities, implies a linear dependence of μ on $T^{3/2}$ at low temperature,[32] clearly observed in Fig. 5(b) at high carrier concentrations ($>10^{14}$ cm^{-2}). The ionized impurities are possibly oxygen vacancies,[33] although whether these can actually act as dopants is still a matter of debate.[34–36]

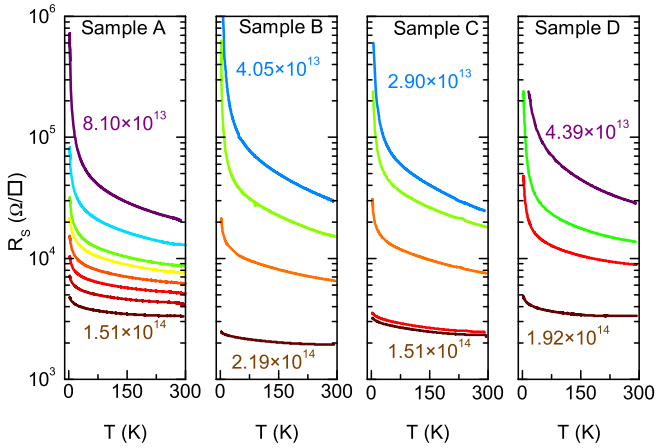

FIG. 4. R_S vs T characteristics in a wide range of doping levels.

B. Magneto-transport

Low temperature magneto-transport can reveal corrections to conductivity arising from classical effects or quantum phase related interference effects. In Fig. 6, we show for samples B and C (circles) the measured normalized correction to the zero field conductivity as a function of the perpendicular applied field for different temperatures [Fig. 6(a)]

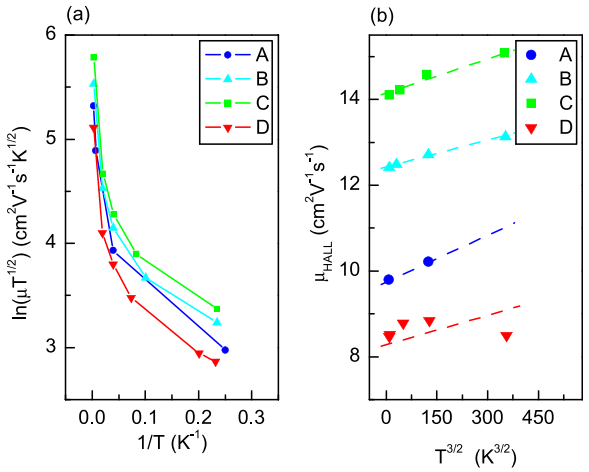

FIG. 5. (a) $\ln(\mu T^{1/2})$ vs $1/T$ plot for the analyzed samples at high doping (in the range of 1.5 to $2.19 \times 10^{14}\,cm^{-2}$), showing that the grain boundary scattering is not the dominant scattering mechanism. (b) μ vs $T^{3/2}$ of the four samples at high doping ($>10^{14}$ cm^{-2}), demonstrating that ionized impurities are the main source of scattering.

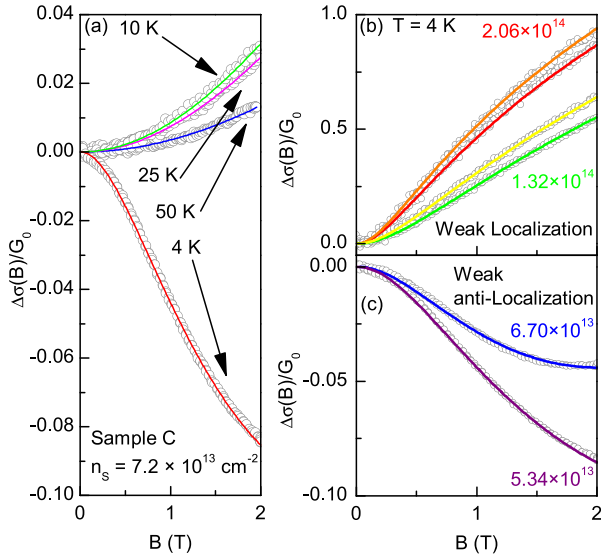

FIG. 6. (a) Correction to the conductivity as a function of the magnetic field for sample C. The carrier density is $7.2 \times 10^{13}\,\mathrm{cm}^{-2}$. WL becomes stronger with decreasing temperature until 10 K. Cooling down to 4 K results in a transition from WL to WAL. (b) $\Delta\sigma(B)/G_0$ for samples B and C as a function of doping at 4 K. As we can see, the transition from the WL to the WAL at a fixed temperature takes place by increasing the doping.

and for different carrier concentrations [Figs. 6(b) and 6(c)]. These are representative of the behaviour in all four samples. Clearly, the correction depends on the magnetic field. At a fixed carrier concentration of 7.2×10^{13} cm^{-2} [Fig. 6(a)], it is negative at 4 K and changes sign to a positive correction at higher temperatures. Similarly, at a fixed temperature of 4 K [Figs. 6(b) and 6(c)], the correction is negative at lower carrier concentrations and changes sign to a positive correction at high carrier concentrations. The order of magnitude of the classical correction to magnetoconductivity can be calculated knowing the mobility and the applied field.[37] In our case, it is negligible. Thus, the observed behaviour is quantum in nature, remarkably observed in polycrystalline materials with relatively low mobility. The positive correction corresponding to *increasing* conductivity with the magnetic field is the weak localization (WL) effect, where constructive interference of closed loop paths favors localization of carriers. This localization is reduced by an applied magnetic field. The negative correction, on the other hand, corresponds to decreasing conductivity with the magnetic field. This is the weak antilocalization (WAL) effect generated by spin-orbit coupling in the material where interference for closed loop paths in opposing directions is now destructive. An applied magnetic field lowers this destructive interference, favouring localization and *decreasing* conductivity. We observe a crossover from WL to WAL as a function of both temperature and carrier concentration. Similar behaviour has been reported in chemically doped ZnO thin films.[11,16,38,39] We now extract meaningful quantities such as characteristic relaxation times by invoking an analytical expression[40,41] for the quantum correction to conductivity as a function of the perpendicular applied magnetic field B

$$\frac{\Delta\sigma(B)}{G_0} = \Psi\left(\frac{1}{2}+\frac{B_\phi + B_{SO}}{B}\right) + \frac{1}{2}\Psi\left(\frac{1}{2}+\frac{B_\phi + 2B_{SO}}{B}\right) - \frac{1}{2}\Psi\left(\frac{1}{2}+\frac{B_\phi}{B}\right) - \ln\left(\frac{B_\phi + B_{SO}}{B}\right) - \frac{1}{2}\ln\left(\frac{B_\phi + 2B_{SO}}{B}\right) + \frac{1}{2}\ln\left(\frac{B_\phi}{B}\right). \quad (3)$$

Ψ is the digamma function, $G_0 = e^2/2\pi^2\hbar$ is the conductance quantum, and $B_\phi = \hbar/4eD\tau_\phi$ and $B_{SO} = \hbar/4eD\tau_{SO}$ are the characteristic fields related to the inelastic scattering time and the spin relaxation time (with $\hbar$ the reduced Planck constant, D the diffusion coefficient, and e the electron charge). $\Delta\sigma(B) = (\sigma(B) - \sigma(0))$, where $\sigma(B)$ and $\sigma(0)$ are the conductivity at field B and the conductivity at $B = 0$, respectively. This expression is an approximation of the more complete formulation[42] and does not explicitly include the total relaxation time τ (corresponding to the mean free path) since we can reasonably assume it to be much smaller than τ_ϕ and τ_{SO}. τ is then obtained from $\tau = \frac{\mu m}{e}$, where μ is the Hall mobility and $m = m_e m_{eff}$ the effective mass of the conduction electrons in ZnO, with $m_{eff} = 0.25$.[43] By fitting $\Delta\sigma(B)/G_0$ with Eq. (3) using B_ϕ and B_{SO} as fitting parameters [solid lines in Fig. 6], we extract τ_ϕ and τ_{SO}. To do so, we use the diffusion coefficient[44] $D = v_F^2\tau/2$, with $v_F = \hbar k_F/m$ the Fermi velocity for an ideal two-dimensional electron gas and a single parabolic conduction band. Typical values obtained for τ corresponding to the mean free path are of the order of 10^{-15} s, justifying the expression used in Eq. (3). In Fig. 7, we show the characteristic fields and relaxation times for the data shown in Fig. 6(a). The error bars in Fig. 7(a), rather than representing statistical error, show the range of variation of the characteristic fields where the fit of the experimental data using Eq. (3) is still valid. For a conservative estimate of the associated relaxation time and its variation, we choose the highest possible value of the characteristic field corresponding to the smallest relaxation time for each temperature or carrier concentration and forego the use

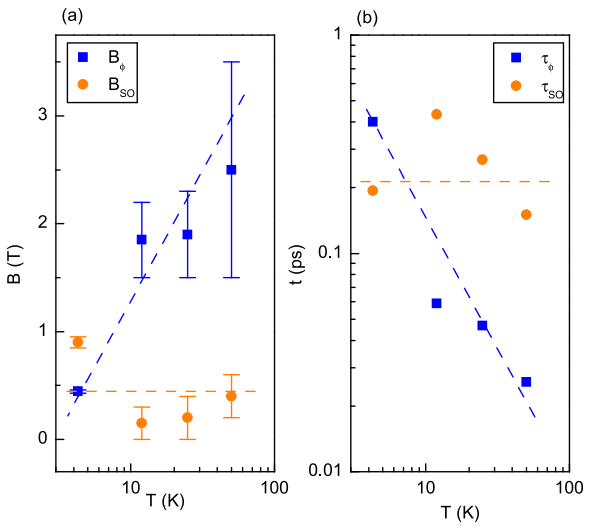

FIG. 7. (a) The variation of B_ϕ and B_{SO} with temperature. (b) Characteristic scattering times as a function of the temperature derived from the values of B_ϕ and B_{SO}.

of error bars in this case. The inelastic scattering time expectedly increases as the temperature decreases and between 10 K and 4 K becomes greater than the spin relaxation time inducing the crossover from WL to WAL [Fig. 7(b)]. We observe that the crossover to WAL occurs at higher temperatures if the doping is decreased, and at a fixed temperature, WAL becomes less pronounced with increasing doping. At extremely high doping ($n_S > 10^{14}$ cm^{-2}), WAL disappears for the temperature range investigated. We can thus modulate the spin relaxation time by tuning the carrier density, with τ_{SO} increasing with increasing carrier density in all samples, as shown in Fig. 8 for the characteristic scattering times obtained from the fit of Figs. 6(b) and 6(c).

The characteristic fields can also be used to obtain the values of the phase-coherence length L_ϕ and the spin-coherence length L_{SO} since $L = \sqrt{D\tau}$, with D the diffusion coefficient and τ the characteristic transport times associated with L. The mean free path at 4 K calculated for the four samples ranges from ~1 nm at the lowest carrier concentration to ~6 nm at the highest carrier concentration. This increase is due to the increasing overlap of the wavefunctions as the carrier concentration increases. At high carrier density, the mean free path is expectedly of the order of the lowest dimension (thickness) of the grain-size. The calculated phase-coherence lengths vary from 16 nm to 49 nm at 4 K when going from low to high carrier concentrations. These values are higher than those of the mean free path and are larger than the minimum dimension of the crystalline grain. For quantum coherence, charge carriers need to remain inside a single crystal grain, for example, along a loop, which is possible, given the disk-like shape of the grains and the average diameter of about 30 nm.

Finally, we seek to understand the dominant mechanism of spin relaxation in our samples. The principal mechanisms to be considered in the presence of spin-orbit coupling are the Elliott-Yafet mechanism,[45,46] the D'Yakonov-Perel' mechanism, and the Rashba-Dresselhaus effect.[47] The D'Yakonov-Perel' mechanism invokes spin-relaxation in systems lacking inversion symmetry, resulting in an effective magnetic field and implying the direct correlation,[47] $\frac{1}{\tau_{SO}} \propto \tau$. However, in Fig. 9(a), we find an inverse correlation excluding this mechanism. Indeed, the D'Yakonov-Perel' mechanism becomes dominant[48] above 50 K, while all our measurements pertain to temperatures below 50 K. Consider now a 2D electron gas doped electrostatically with a perpendicular electric field. Spin-orbit coupling is directly proportional to the electric field and thus to the carrier density, implying[47] $B_{SO} \propto n_s$ in the case of the Rashba-Dresselhaus effect. In Fig. 9(b), we show the relationship between these two quantities at 4 K. Again, an inverse proportionality is seen invalidating this effect in our samples. In the Elliott-Yafet mechanism, spin relaxation is caused by scattering from ions of the lattice, from impurities or from phonons. At every scattering event, there is a finite probability that the electron changes its spin orientation, implying $\tau_{SO} \propto \tau$. It is reasonable to think that this mechanism is active in our samples containing oxygen vacancies as scattering centers. In Fig. 10, we show the relationship between τ_{SO} and τ at 4 K. Here, the expected direct proportionality is observed, indicating that this is the dominant mechanism of spin relaxation in our samples.

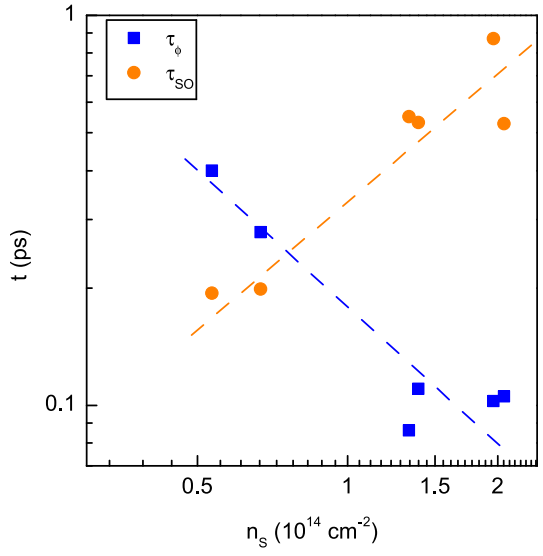

FIG. 8. Evolution of the characteristic scattering times τ_ϕ and τ_{SO} as a function of the carrier density.

IV. CONCLUSIONS

Polycrystalline thin films of ZnO_{1-x}(<40 nm) were fabricated on glass substrates using magnetron sputtering, and their carrier density was modulated using our space charge doping technique. The maximum carrier density attained

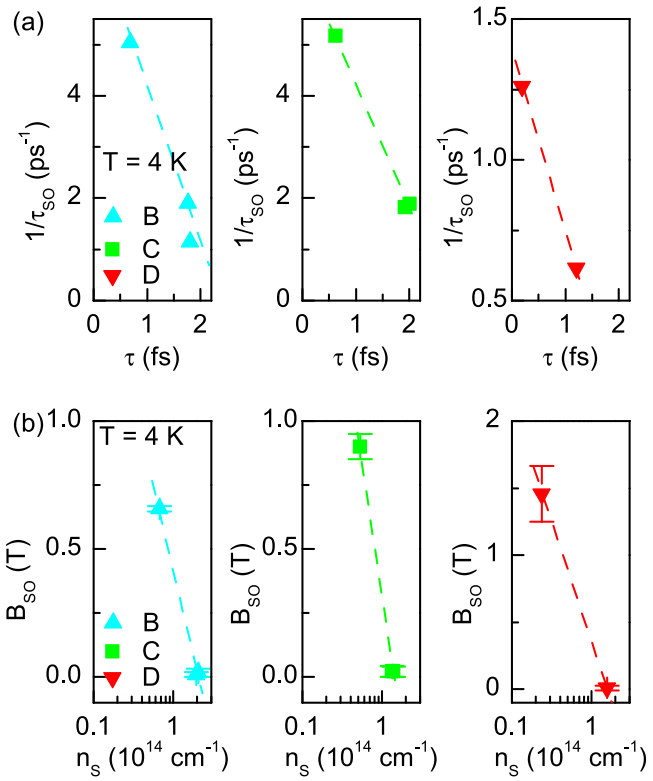

FIG. 9. (a) Variation of $1/\tau_{SO}$ with respect to τ showing an inverse correlation between the two quantities and invalidating the D'Yakonov-Perel' mechanism in our samples. (b) Dependence of the term B_{SO} as a function of the carrier density measured at 4 K. Again, the inverse correlation invalidates the Rashba-Dresselhaus effect.

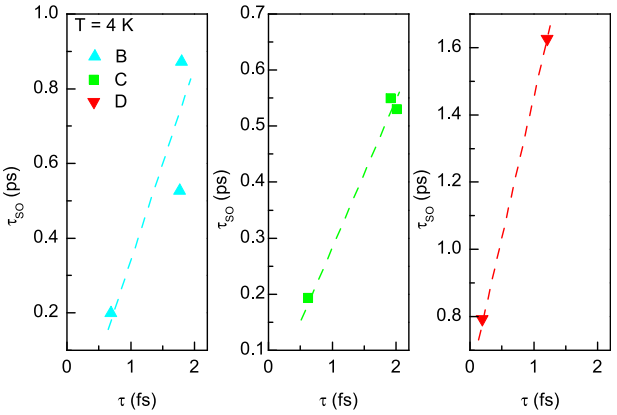

FIG. 10. Variation of τ_{SO} as a function of τ at 4 K. The proportional relationship between the two characteristic times demonstrates that the Elliot-Yafet mechanism is dominant in our system.

was $2.2 \times 10^{14}\,\mathrm{cm}^{-2}$ with a minimum sheet resistance of the order of $2\,\mathrm{k}\,\Omega/\square$. The doping level can be finely controlled by the space charge in the accumulation layer at the interface, allowing us to study the electronic properties of the thin-film in a wide range of carrier concentrations. Such electrostatically doped ZnO thin films could have potential applications as a transparent conducting electrode. The analysis of the Hall mobility in the 4–50 K range at various doping levels showed that the main scattering mechanism for electrons is by charged impurities, probably the oxygen vacancies in the film. We could observe quantum interference phenomena in the low temperature magnetoconductivity of these films and extract characteristic values related to the scattering mechanisms. Our analysis revealed that the same impurities are responsible for spin relaxation in the system. We observe a remarkable transition from weak localization to weak anti-localization under certain conditions and show that it is possible to modulate spin relaxation time by tuning the carrier density. Future potential applications of SCD applied to ZnO could be the study of p conductivity.

ACKNOWLEDGMENTS

This work was partially supported by ANR SUPERTRAMP and Labex MATISSE. The authors thank J.-Y. Duquesne for the assistance in the deposition of thin films. We thank F. Gendron, J.-L. Cantin, and J. Von Bardeleben for access to electromagnet facility. We thank L. Becerra, M. Escudier, M. Rosticher, and J. Palomo for help with clean room facilities.

[1]A. Janotti and C. G. Van de Walle, "Fundamentals of zinc oxide as a semiconductor," Rep. Prog. Phys. **72**(12), 126501 (2009).
[2]U. Ozgur, Y. I. Alivov, C. Liu, A. Teke, M. A. Reshchikov, S. Dogan, V. Avrutin, S. J. Cho, and H. Morkoc, "A comprehensive review of ZnO materials and devices," J. Appl. Phys. **98**(4), 041301 (2005).
[3]E. M. C. Fortunato, P. M. C. Barquinha, A. C. M. B. G. Pimentel, A. M. F. Gonçalves, A. J. S. Marques, L. M. N. Pereira, and R. F. P. Martins, "Fully transparent ZnO thin-film transistor produced at room temperature," Adv. Mater. **17**(5), 590–594 (2005).
[4]P. F. Garcia, R. S. McLean, M. H. Reilly, and G. Nunes, "Transparent ZnO thin-film transistor fabricated by rf magnetron sputtering," Appl. Phys. Lett. **82**(7), 1117 (2003).
[5]A. a. Mosquera, D. Horwat, A. Rashkovskiy, A. Kovalev, P. Miska, D. Wainstein, J. M. Albella, and J. L. Endrino, "Exciton and core-level electron confinement effects in transparent ZnO thin films," Sci. Rep. **3**, 1714 (2013).
[6]X. Jiang, F. L. Wong, M. K. Fung, and S. T. Lee, "Aluminum-doped zinc oxide films as transparent conductive electrode for organic light-emitting devices," Appl. Phys. Lett. **83**(9), 1875 (2003).
[7]D. Eger, A. Many, and Y. Goldstein, "Quantum properties of strong accumulation layers on ZnO surfaces," Surf. Sci. **58**(1), 18–24 (1976).
[8]T. Minami, H. Nanto, and S. Takata, "Highly conductive and transparent aluminum doped zinc oxide thin films prepared by RF magnetron sputtering," Jpn J. Appl. Phys., Part 2 **23**(1), L280–L282 (1984).
[9]A. E. Jiménez-González, J. A. Soto Urueta, and R. Suárez-Parra, "Optical and electrical characteristics of aluminum-doped ZnO thin films prepared by solgel technique," J. Crystal Growth **192**(3–4), 430–438 (1998).
[10]M. Chen, Z. L. Pei, X. Wang, C. Sun, and L. S. Wen, "Structural, electrical, and optical properties of transparent conductive oxide ZnO:Al films prepared by dc magnetron reactive sputtering," J. Vac. Sci. Technol. A **19**(3), 963 (2001).
[11]T. Andrearczyk, J. Jaroszyński, G. Grabecki, T. Dietl, T. Fukumura, and M. Kawasaki, "Spin-related magnetoresistance of n-type ZnO:Al and $Zn1_xMn_xO$:Al thin film," Phys. Rev. B **72**(12), 121309 (2005).
[12]I. A. Buyanova, A. Murayama, T. Furuta, Y. Oka, D. P. Norton, S. J. Pearton, A. Osinsky, J. W. Dong, C. W. Tu, and W. M. Chen, "Spin Dynamics in ZnO-Based Materials," J. Supercond. Novel Magn. **23**(1), 161–165 (2010).
[13]Y. Shapira, "Anomalous effect of UHV-component-generated atomic hydrogen on the surface properties of ZnO," J. Vac. Sci. Technol. **13**(2), 615 (1976).
[14]G. Yaron, A. Many, and Y. Goldstein, "Quantized electron accumulation layers on ZnO surfaces produced by low-energy hydrogen-ion implantation," J. Appl. Phys. **58**(9), 3508 (1985).
[15]Y. Goldstein, A. Many, D. Eger, Y. Grinshpan, G. Yaron, and M. Nitzan, "Extreme accumulation layers on ZnO surfaces due to He+ ions," Phys. Lett. A **62**(1), 57–58 (1977).
[16]A. Goldenblum, V. Bogatu, T. Stoica, Y. Goldstein, and A. Many, "Weak localization effects in ZnO surface wells," Phys. Rev. B **60**(8), 5832–5838 (1999).
[17]H. Yuan, H. Shimotani, A. Tsukazaki, A. Ohtomo, M. Kawasaki, and Y. Iwasa, "High-density carrier accumulation in ZnO field-effect transistors gated by electric double layers of ionic liquids," Adv. Funct. Mater. **19**(7), 1046–1053 (2009).
[18]H. Yuan, H. Shimotani, J. Ye, S. Yoon, H. Aliah, A. Tsukazaki, M. Kawasaki, and Y. Iwasa, "Electrostatic and electrochemical nature of liquid-gated electric-double-layer transistors based on oxide semiconductors," J. Am. Chem. Soc. **132**(51), 18402–18407 (2010).
[19]B. Y. Oh, M. C. Jeong, T. H. Moon, W. Lee, J. M. Myoung, J. Y. Hwang, and D. S. Seo, "Transparent conductive Al-doped ZnO films for liquid crystal displays," J. Appl. Phys. **99**(12), 124505 (2006).
[20]A. Paradisi, J. Biscaras, and A. Shukla, "Space charge induced electrostatic doping of two-dimensional materials: Graphene as a case study," Appl. Phys. Lett. **107**(14), 143103 (2015).
[21]J. Biscaras, Z. Chen, A. Paradisi, and A. Shukla, "Onset of two-dimensional superconductivity in space charge doped few-layer molybdenum disulfide," Nat. Commun. **6**, 8826 (2015).
[22]H. Mehrer, A. W. Imre, and E. Tanguep-Nijokep, "Diffusion and ionic conduction in oxide glasses," J. Phys.: Conf. Ser. **106**, 012001 (2008).
[23]E. M. C. Fortunato, P. M. C. Barquinha, A. C. M. B. G. Pimentel, A. M. F. Goncalves, A. J. S. Marques, R. F. P. Martins, and L. M. N. Pereira, "Wide-bandgap high-mobility ZnO thin-film transistors produced at room temperature," Appl. Phys. Lett. **85**(13), 2541 (2004).
[24]E. Ziegler, A. Heinrich, H. Oppermann, and G. Stöver, "Electrical properties and non-stoichiometry in ZnO single crystals," Phys. Status Solidi A **66**(2), 635–648 (1981).
[25]Y. M. Lu, W. S. Hwang, W. Y. Liu, and J. S. Yang, "Effect of RF power on optical and electrical properties of ZnO thin film by magnetron sputtering," Mater. Chem. Phys. **72**(2), 269–272 (2001).
[26]G. G. Rusu, M. Grtan, and M. Rusu, "Preparation and characterization of ZnO thin films prepared by thermal oxidation of evaporated Zn thin films," Superlattices Microstruct. **42**(1–6), 116–122 (2007).
[27]A. L. Patterson, "The Scherrer formula for X-ray particle size determination," Phys. Rev. **56**(10), 978–982 (1939).
[28]S. Das Sarma and E. H. Hwang, "Two-dimensional metal-insulator transition as a strong localization induced crossover phenomenon," Phys. Rev. B **89**(23), 235423 (2014).

[29]A. T. Vai, V. L. Kuznetsov, H. Jain, D. Slocombe, N. Rashidi, M. Pepper, and P. P. Edwards, "The transition to the metallic state in polycrystalline n-type doped ZnO thin films," Z. Anorg. Allg. Chem. **640**(6), 1054–1062 (2014).
[30]D. H. Zhang and H. L. Ma, "Scattering mechanisms of charge carriers in transparent conducting oxide films," Appl. Phys. A: Mater. Sci. Process. **62**(5), 487–492 (1996).
[31]R. L. Petritz, "Theory of photoconductivity in semiconductor films," Phys. Rev. **104**(6), 1508–1516 (1956).
[32]S. A. Agnihotry, K. K. Saini, T. K. Saxena, K. C. Nagpal, and S. Chandra, "Studies on e-beam deposited transparent conductive films of In 2 O 3: Sn at moderate substrate temperatures," J. Phys. D: Appl. Phys. **18**(10), 2087–2096 (1985).
[33]J. Robertson and S. J. Clark, "Limits to doping in oxides," Phys. Rev. B **83**(7), 075205 (2011).
[34]A. Alkauskas and A. Pasquarello, "Band-edge problem in the theoretical determination of defect energy levels: The O vacancy in ZnO as a benchmark case," Phys. Rev. B **84**(12), 125206 (2011).
[35]L. Liu, Z. Mei, A. Tang, A. Azarov, A. Kuznetsov, Q. Xue, and X. Du, "Oxygen vacancies: The origin of n-type conductivity in ZnO," Phys. Rev. B **93**(23), 235305 (2016).
[36]L. S. Vlasenko and G. D. Watkins, "Optical detection of electron paramagnetic resonance in room-temperature electron-irradiated ZnO," Phys. Rev. B **71**(12), 125210 (2005).
[37]G. Giuliani, "A general law for electromagnetic induction," EPL (Europhys. Lett.) **81**(6), 60002 (2008).
[38]D. F. Wang, J. M. Kim, M. S. Seo, V. T. T. Thuy, Y. J. Yoo, Y. P. Lee, and J. Y. Rhee, "Magnetoresistance in ZnO induced by spin-splitting and weak localization," Mater. Chem. Phys. **134**(1), 74–79 (2012).
[39]D. F. Wang, Y. Ying, V. T. T. Thuy, J. M. Kim, M. S. Seo, F. Gao, T. J. Zhang, K. W. Kim, and Y. P. Lee, "Temperature-dependent magnetoresistance of ZnO thin film," Thin Solid Films **520**(1), 529–532 (2011).
[40]G. E. Iordanskii, S. V. Lyanda-Geller, and Y. B. Pikus, "Weak localization in quantum wells with spin-orbit interaction," JETP Lett. **60**, 206 (1994), available at http://www.jetpletters.ac.ru/ps/1323/article_20010.shtml.
[41]A. D. Caviglia, M. Gabay, S. Gariglio, N. Reyren, C. Cancellieri, and J. M. Triscone, "Tunable Rashba spin-orbit interaction at oxide interfaces," Phys. Rev. Lett. **104**(12), 126803 (2010).
[42]S. Hikami, A. I. Larkin, and Y. Nagaoka, "Spin-orbit interaction and magnetoresistance in the two dimensional random system," Prog. Theor. Phys. **63**(2), 707–710 (1980).
[43]H. Morkoç and Ü. Özgür, *Zinc Oxide: Fundamentals, Materials and Device Technology* (John Wiley & Sons, 2008).
[44]A. V. Germanenko, "Spin effects and quantum corrections to the conductivity of two-dimensional systems," Low Temp. Phys. **35**(1), 24 (2009).
[45]R. J. Elliott, "Theory of the effect of spin-orbit coupling on magnetic resonance in some semiconductors," Phys. Rev. **96**(2), 266–279 (1954).
[46]Y. Yafet, "g factors and spin-lattice relaxation of conduction electrons," Solid State Phys. **14**, 1–98 (1963).
[47]I. Žutić, J. Fabian, and S. Das Sarma, "Spintronics: Fundamentals and applications," Rev. Mod. Phys. **76**(2), 323–410 (2004).
[48]N. J. Harmon, W. O. Putikka, and R. Joynt, "Theory of electron spin relaxation in ZnO," Phys. Rev. B **79**(11), 115204 (2009).